An Integrated Multiscale Geometric Analysis Approach for Automatic Extraction of Power Lines From High Resolution Remote Sensing Images

MULETA EBISSA FEYISSA[1], **JIANNONG CAO**[1], **AND JUNJUN LI**[2]

[1]College of Geological Engineering and Surveying, Chang'an University, Xi'an 710064, China
[2]School of Earth Science and Resources, Chang'an University, Xi'an 710064, China

Corresponding author: Jiannong Cao (caojiannong@126.com)

ABSTRACT High resolution remote sensing systems provide cheaper and fast way of acquiring images of power lines. However, such images depicting the details of other complex background objects, noises, and complicated brightness measurements, make separate extraction of the power lines challenging. This paper addresses the problem of automatic extraction of power lines from high resolution remote sensing images obtained from different sources. In order to automatically extract the power lines, we proposed an integrated Multiscale Geometric Analysis (MGA) approach. First, complementary Gabor and matched filters (MF) were employed over an image to suppress unnecessary background and noises, and initial discrimination of the power lines. Then, the filtering output was decomposed in to scale and orientation based subband coefficients using the Fast Discrete Curvelet Transform (FDCT) so as to access and modify different image features separately. By employing selective modification operations, well-established power line structures ready for extraction were derived. Finally the powerlines were extracted with hysteresis thresholding. The approach was successful in extracting power lines from high resolution images captured in any orientation. It is robust even when the source image is cluttered, and degraded due to noise and brightness effects. Power lines represented by weak intensities, crossing bright image regions, changing direction, closer power lines and those crossing each other, disconnected/broken power lines due to noise and occlusions were all inferred and extracted successfully. The approach was validated using real test images and the performance measures showed over 90% average accuracy fitting the ground truth.

INDEX TERMS Automatic extraction, high resolution, MGA, remote sensing image, power line.

I. INTRODUCTION

Power lines are important components of our daily lives. They need regular maintenance and emergency repairs. Conducting ground surveying for inspection is labor intensive, time consuming and expensive [1]. Satellites and aerial vehicles provide cheaper and fast ways of inspecting them. They allow capturing the images of the power lines remotely [2]. They provide potentials for automatic extraction of the power lines so as to derive fast and up-to-date information. Power lines are too small to be depicted as images remotely [3], [4] and thus require high resolution spaceborne or airborne sensors. However, these fine resolution sensors capture the fine details of other objects by mixing up with the power lines. They capture the details of terrain features, both natural and man-made, at a time by the same sensor with similar scale, energy and orientation regardless of size or orientation of those objects. These make power line extraction challenging and costy.

There have been studies conducted on extracting power lines from high resolution remotely sensed images. Most of the existing approaches were employed on aerial images. Some of these approaches used specific filtering and image transformation methods. In [5], line and ratio line detectors

M. E. Feyissa *et al.*: Integrated MGA Approach for Automatic Extraction of Power Lines From High Resolution Remote Sensing Images

IEEE *Access*

were proposed to detect and extract candidate power line pixels from images captured onboard helicopter. The Radon transform and Kalman filter were then employed over the extracted candidates to derive the power lines. In [6], a specifically designed filter named pulse coupled neural network filter (PCNF) was proposed. The filter was applied over an UAV image to discriminate pixels representing the power lines. Then, the Hough transform was used to extract the power lines.

A Series of power line detection algorithms named PLineD detectors were proposed by [7]. First, EDLine detector and Edge Drawing algorithms were utilized to detect edge lines and extract segments. Then, Segments Cut and Segment Covariance algorithms were used to select candidate line segments followed by selective preserving of segments using Group Segments algorithm. Finally, the Parallel Segments algorithm was used to form the power lines. In [8] power line extraction from UAV images was carried out based on edge information. First, image gradient was derived and followed by Otsu based thresholding. Subsequently, the Hough transform was applied to extract straight lines. Finally using the K-means clustering, the power lines were filtered. The Kalman filter was employed for tracking the detected power lines.

Gabor filtering and Hough transform based power lines extraction was carried out by [9]. First, Gabor filtering was employed to remove background noises and then the Hough transform was applied for straight-line fitting and power line extraction. The extraction of power lines from high resolution satellite image (the GeoEye-1) and Google Earth imagery has also been introduced [3]. The authors first employed Curvelet transform to enhance the power lines and then edge detection was used. Finally, the powerlines were extracted using an improved Radon transform.

A number of morphological filtering based approaches were also proposed to extract power lines from UAV derived images. In [10] morphological filters were employed over matched filtering and first order derivative of Gaussian (FDOG). A Clustering and morphological operations were also established for power line extraction [11]. The approach involves DaviesBouldin (DB) index based K-means clustering, morphological skeletonisation, and region growing operations followed by the application of geometrical shape and density index application.

A geometric relationship based approach called the Circle Based Search (CBS) was employed for power line extraction [12]. It was implemented over the output of Canny edge detection and steerable filtering.

Photogrammetric approaches were also employed to extract power lines from UAV images. In [13] epipolar constraints based power line automatic measurement and semi patch matching methods were used in extracting 2D and 3D power lines from epipolar images. A 3D power lines extraction method from aerial images was also proposed using photogrammetric parameters, filtering and cubic grid points [2].

There are some limitations with the existing methods. Some of them are not sufficient to extract power lines from low contrast and very bright image regions. Others fail to detect the power lines enough from complex back ground, and unable to discriminate them from similar parallel linear objects. Moreover, most of the proposed approaches were employed over aerial images obtained from photogrammetric planned flight missions. This could be due to the image resolution and power line's relative finer diameter. In such cases, the image capturing process is adjusted so as to obtain optimum illumination of the power lines. Such approaches may work well only for images obtained from planned flight. A potential approach is demonstrated in [3] that it is of great importance to extend and improve automatic power line extraction from any aerial or space based images taken in any orientation given that the images render power lines information.

This paper proposes a MGA method of automatic extraction of power lines from high resolution images of any source captured at any orientation. It is an approach in which image features are accessed at several scales and orientations, and selectively investigated. The work is part of the efforts to address the existing problems and provide a novel approach of extracting power lines automatically. It is robust even in the presence of background noise, effective over low contrast image regions and resist brightness effects. The method can successfully extract connected power lines oriented to different directions.

The remaining part of the paper is outlined as follows. Section II consists of the theoretical background and the procedures of the methodology. Section III describes the implementation of the proposed method. Section IV describes the experimental results with discussions. Conclusions of the work are given in section V.

II. METHODOLOGY

The proposed approach comprises of three steps (Fig. 1). In the first step, two complementary filters were used to enhance the power lines and suppress the unnecessary background. First, a bank of Gabor filters was defined using appropriate parameters and followed by convolving with an input image. Then the Gabor response subbands with optimum information content were selected and maximally combined. Consequently, the output was convolved with a defined (MF).

In the second step, the filtering output of the first step was decomposed in to multiscale and multiorientation Curvelet coefficients using FDCT. Then, the coefficients representing image objects were selectively accessed and modified in a way that the power line representing coefficients are preserved and enhanced. Subsequently, the image was recovered using inverse FDCT. The third step involves the extraction and refinement of the power lines from the output of the Curvelet transform. In this step, the hysteresis thresholding was first used to segment the power lines and then morphological operations were used to refine the extraction. The whole experiment was conducted using MATLAB.
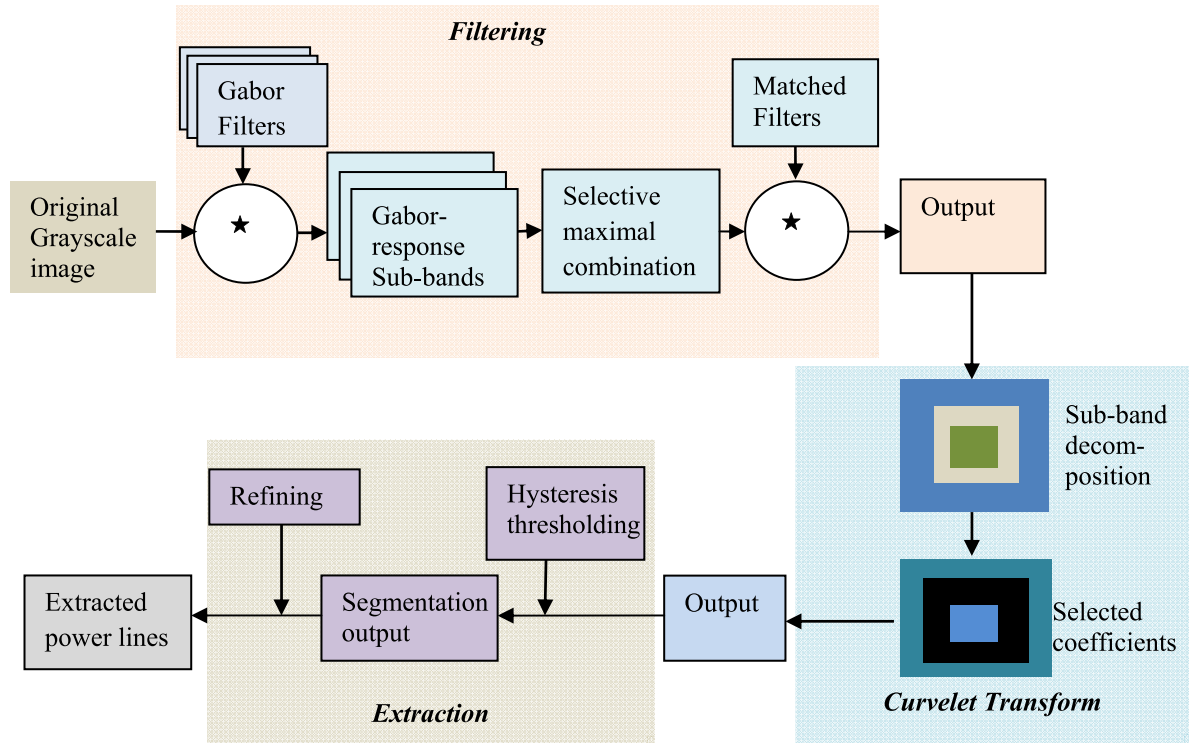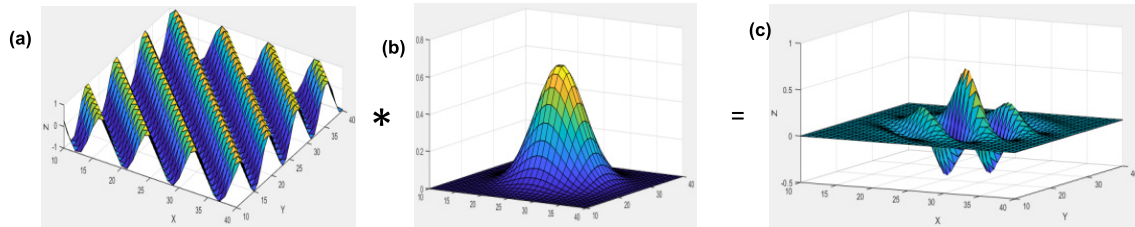
FIGURE 1. Schematic view of the proposed approach.

FIGURE 2. Visualization of 2D gabor filter (a) the sinusoidal wave, (b) the gaussian c) the gabor filter.

A. FILTERING WITH GABOR FUNCTION

Remotely sensed high resolution images are commonly associated with complex background and noises. Thus, selective preserving and enhancement of the structures of target feature/s is a crucial procedure. Gabor filtering is an effective approach for image objects discrimination and information preservation with multiscale and multidirection tunable potentials [14]. It has been successfully applied to a wide range of image processing applications. In [14]–[16], the Gabor filters were employed for unsupervised image segmentation. Recent studies show that the Gabor functions are gaining momentum in processing remote sensing images. Gabor filters were used to detect buildings ([17] and land cover changes [18], and extract roads [19] from high resolution optical images. In [20], texture features from radar images were extracted with Gabor function and the output was used to identify rain and backscatter regions effectively.

The Gabor function is a Gaussian envelope modulated by sinusoidal plane wave of complex exponential (cosine or sine) functions at specific frequency and orientation [21]. For simplicity, assuming that the rotation of the Gaussian and the sinusoidal are the same, a 2D Gabor filter is presented in Fig. 2.

In [22]–[24], the normalized 2D Gabor function is defined mathematically in the spatial domain as (1).

$$\psi_{f,\theta}(x,y) = \frac{f^2}{\pi \gamma \eta} e^{-f^2\left[\left(\frac{x'}{\gamma}\right)^2 + \left(\frac{y'}{\eta}\right)^2\right]} e^{j2\pi fx'} \tag{1}$$

where $\psi_{f,\theta}(x,y)$ is the Gaussian modulated by a complex sinusoid, x and y are the positions in space, f is the central frequency (*cycles/pixel*), θ is the rotation angle, γ and η are the width along the major and minor axis, respectively; $x' = x\cos\theta + y\sin\theta$ and $y' = -x\sin\theta + y\cos\theta$.

Equation (1) produces a specific band pass ellipse shaped Gabor filter with specific location and orientation centered at (f, θ) with axis length proportional to a given frequency bandwidth (FBW) and aspect ratio (AR). However, the

representation of complex objects in images rather needs spatial constellations of several multiresolution Gabor filters.

Thus, self-similar several multi-resolution and multidirection Gabor filters with varying central frequency and orientations are derived [25], [26] as:

$$\psi_{mn}(x, y) = a^{-m} \psi(\tilde{x}, \tilde{y}) \tag{2}$$

where m and n denote filter's scale and orientation, respectively; $m = 0, 1, \ldots M - 1, n = 0, 1, \ldots N - 1$, and M and N are the total number of scale and orientation, respectively; $\tilde{x} = a^{-m}(x\cos\theta + y\sin\theta)$ and $\tilde{y} = a^{-m}(-x\sin\theta + y\cos\theta)$ represents the dilation of the mother Gabor filter $\psi(x, y)$ by a scaling factor a^{-m} and rotation by $\theta = n\nabla\theta$.

In constructing a bank of Gabor filters, the possible combination of the parameters (f, θ, γ and η) determines the total number of Gabor filters and how the filter captures the target features properly. The total number of the required Gabor filters is derived from the product of the preferred total numbers of orientation (θ) and the frequency (f).

Multiscale center frequencies are computed from the possible total number of the center frequencies. The possible total number of f for a square image of size $N \times N$ where N is a power of 2 is defined in [14] as $log_2(N/2)$. Then, specific values of f are generated from a given regularly spaced wavelengths defined in pixels in increasing order. This is given as $\sqrt{2}/2\lambda$, where λ denotes a given wavelength.

By fixing the desired highest frequency (f_{max}) value, each of the radial frequency values can be drawn [22], [24], [27]. This is given as:

$$f_k = a^{-k} f_{max}, \quad k = \{0, \ldots M - 1\} \tag{3}$$

where f_k is the kth bin frequency, $f_{max} = f_0$ is the desired highest frequency, M is total number of scales; a is frequency scaling factor and can be 2 for octave spacing and $\sqrt{2}$ for half octave spacing.

With respect to orientation, it is commonly assumed that the spacing of the orientations of Gabor filters is isotropic and takes a dyadic approach to cover the spatial frequency nearly uniformly [22]. This is determined as:

$$\theta_k = \frac{k\pi}{N} \quad \text{for } k = 0, \ldots N - 1 \tag{4}$$

where θ_k is the kth orientation and N is the total number of orientations in radians

The AR and the FBW parameters control the effective areas of Gabor filters. The AR is the ratio of the major axis (γ) to the minor axis (η) of the Gaussian. The value specifies the ellepticity of the Gaussian support and can control sharpness. The value $\eta = \gamma = 1$ represent circular shape and $\eta < \gamma$ represents unequal dimensional objects in an image. The FBW is the half response spatial frequency bandwidth of a Gabor filter relating to the ratio of the standard deviation of Gaussian factor of the Gabor function and the wavelength of the cosine part of the Gabor filter described in pixels.
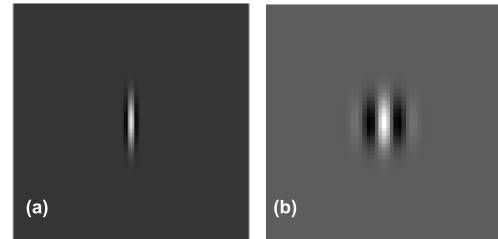
FIGURE 3. Gabor filter spatial kernels at $f = 0.88$ and $\theta = 0^0$; (a) FBW=2.5 and AR=0.2, (b) FBW=1.2 and AR=0.9.

Both the FBW and AR are application dependent parameters. They can optimally be adjusted to encapsulate the event of interest [23], [28]. Typical values are in the range of [0.25, 1] for AR and [0.5 − 2.5] for FBW [21], [15]. Fig. 3 presents two samples of Gabor filter kernels. Both filters have the same central frequency ($f = 0.88$) and the same orientation ($\theta = 0^0$). While Fig. 3(a) is derived from FBW = 2.5 and AR = 0.2, Fig. 3(b) is derived from FBW = 1.2 and AR = 0.9.

It is clearly visible that the Gabor filter kernel with lower AR but higher FBW provide thinner and longer range higher amplitude Gabor coefficients suitable for linear objects enhancement.

Once, the required Gabor filter $\psi_{f,\theta}(s, t)$ is defined enough, the input image $I(x, y)$ is convolved by the 2D Gabor to obtain the Gabor response image [27].

$$r_{f,\theta}(x, y) = \psi_{f,\theta}(s, t) * I(x, y) \tag{5}$$

where $r_{f,\theta}(x, y)$ is the Gabor response, s and t are the filter mask coordinates at f and θ.

From the generated Gabor image response, one can consider either all or select the optimum subband/s which be able to distinguish the target object from the other background objects.

The magnitude of the Gabor response is commonly used to determine the optimum Gabor image space [29]. The magnitude at each scale and orientation of the Gabor image space is computed automatically as a summation of the absolute value of each filtered sub-image [26] as:

$$E_{(m,n)} = \sum_x \sum_y |G_{mn}(x, y)| \tag{6}$$

where m is the scale and n is orientation with $m = 0, 1, \ldots, M - 1$ and $n = 0, 1, \ldots, N - 1$

From the obtained outputs, the required optimum subbands can then be selected and fused maximally.

B. THE MATCHED FILTERING OF THE GABOR IMAGE SPACE

Although the Gabor filter can reduce the influence of the background objects and enhance the target objects based on the defined parameters, it may not be sufficient to explicitly represent the geometric structures of target features from high resolution images associated with different ill-posed
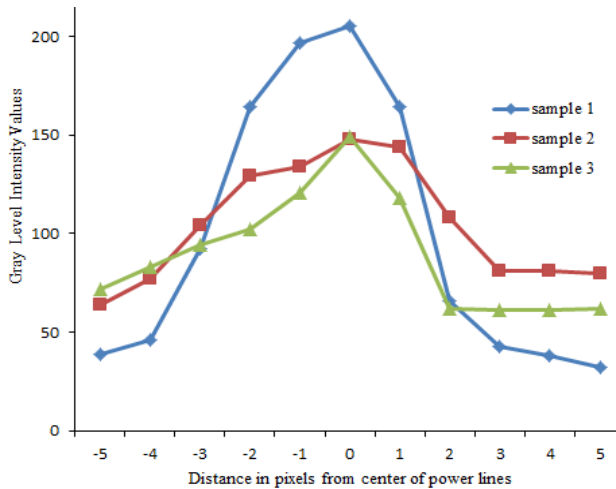
FIGURE 4. Profiles of the cross-section of three sample power lines in an image.

problems. Moreover, the maximal combination of the different oriented filter responses can introduce some unnecessary noises. Thus, complementary filters that can further suppress the background noises and amplify the structures of the power lines are desirable. One of such approaches is to use MF.

The MFs are templates of discrete functions whose impulse responses are similar to the shape of a target object in a signal or image. A MF is derived from the point of view of maximizing output amplitudes or can arbitrarily be chosen in correspondence with the details of the object to be detected or extracted [30].

MF have widely been used in processing $1 - D$ signals as in communication systems [31]. Inspired by the $1 - D$ applications, researchers extended template object detection to image object manipulations. The applications in image processing includes texture discriminations and target object tracking [32], seismic imaging and event detections [33], [34], medical analysis [35]–[37], and feature extraction [38].

The Gaussian function is considered as suitable template to approximate features in images based on shapes. In [36]–[38], the Gaussian template was used to approximate vessel structures in medical images. Such filters are adaptable to approximate linear features having Gaussian nature in remotely sensed images. The power lines are of such features. They possessed properties like higher reflectance than their background and intensity profile similar to Gaussian shape (Fig. 4). These properties can be modelled with the Gaussian template.

The Gaussian MF is the matching of Gaussian template to an image where the template is a sub-image that contains the target object's shape in the image [39].

This is defined in [35], [36] as:

$$f(x, y) = \frac{1}{\sqrt{2\pi\sigma}} \exp\left(-\frac{x^2}{2\sigma^2}\right) - m,$$
$$\forall \, |x| \le t\sigma, \quad |y| \le L/2 \quad (7)$$

where L is the length of the structure to be detect, σ defines the spread of the intensity profile, t is a constant that defines the position where the Gaussian curve trails will cut. For more than 99% of the area under the Gaussian curve lies within the range of $[-3\sigma, 3\sigma]$), t is usually set to 3 [37]. And m is the normalizing value so as the filter has zero mean. It is derived as in (8).

$$m = \left(\int_{-t\sigma}^{t\sigma} \frac{1}{\sqrt{2\pi\sigma}} \exp\left(-\frac{x^2}{2\sigma^2}\right) dx \right) \Big/ (2t\sigma) \quad (8)$$

For structures appearing at different orientations, the Gaussian kernel is required to rotate to be able to detect all possible orientations.

The rotation angle (θ_n) is determined as:

$$\theta_n = n \cdot (\pi/M) \in [0, \pi), \quad \text{where } n = 0, \dots, M - 1 \quad (9)$$

where θ_n is the nth orientation and M is the total number of orientations in degrees

A number of directional filters can be derived by rotating from one coordinate system (x, y) to another (u, v) using geometric transformation:

$$k_i = [u \ v] = [x \ y] \begin{bmatrix} \cos\theta_n & -\sin\theta_n \\ \sin\theta_n & \cos\theta_n \end{bmatrix} \quad (10)$$

where k_i is the number of directional filters (Fig. 5).

The neighborhood N is defined as:

$$N = \{(u, v), |u| \le 3\sigma, |v| \le L/2\} \quad (11)$$

The filter response is obtained by convolving the oriented kernels k_i with the input image $I(x, y)$ followed by computing maximum response over all orientations.

C. THE CURVELET TRANSFORM OF THE MF-GABOR IMAGE SPACE

Due to the complex nature of high resolution images, the fineness of power lines and the maximal combination of multi oriented Gabor filters, resistant noises can still exist. Moreover, some structures of the power line can still left weak due to image degradations. In order to extract accurate geometrical information from the Gabor-MF response image, those limits are required to be selectively fixed. This seeks a method of approaching the image at series of disjoint scales and orientations.

A MGA tool called the Curvelet transform decomposes an image in to different scales and orientations, and represent an image as Curvelet coefficients. Based on the magnitude of the coefficients, any of the scales and the corresponding angles are selected, examined and modified to come up with the required output. The method allows accessing the structures via their belonging scale and orientation. It opens a way to choose only those structures of certain length to be kept and to suppress all the other structures and noises. It has been applied for seismic data exploration [40], medical image processing [41], [42], optical image denoising and edge preservation [43], image enhancements [44], automated
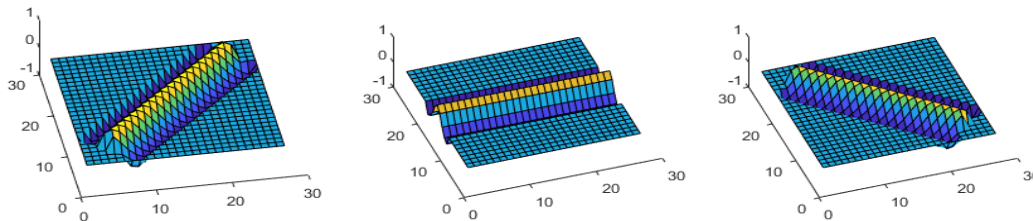
M. E. Feyissa *et al.*: Integrated MGA Approach for Automatic Extraction of Power Lines From High Resolution Remote Sensing Images

IEEE *Access*

FIGURE 5. Sample matching filters oriented to three directions $\left(\theta = 45^0, 90^0 \text{ and } 135^0\right)$ at $\sigma = 2; L = 47$.

change analysis [45] and object detection [46] from SAR images.

The Curvelet transform is a frame of wave packet on $L^2\left(\mathbb{R}^2\right)$. Its definition begins with the construction of a mother Curvelet (φ). The translation, scaling and rotation of this mother Curvelet generate the curvelet frame. The elements of the translated, scaled and rotated Curvelet family provide a partitioned 2D plane [47]. The comprehensive mathematical theory is given in [47], [48]. To draw a basic background for our analysis, a Curvelet is defined in the continuous domain using spatial variable (x), frequency variable (ω), the frequency domain polar coordinates (r, θ), and two none negative real valued windows: the radial (W) and angular (V) windows. A polar wedge represented by U_j supported by the radial $\{W(r)\}$ and angular $\{V(r)\}$ windows can then be generated as a function of scale (j) and orientation (θ) in the Fourier domain (12).

$$U_j(r, \theta) := 2^{\frac{-3j}{4}} W\left(2^{-j}r\right) V\left(\left(2^{\lfloor j/2 \rfloor}\theta\right)/2\pi\right),$$
$$r \geq 0, \quad \theta \in [0, 2\pi), j \in \mathbb{N}_0 \quad (12)$$

where $\mathbb{N}_0$ denotes the number of scales

The spatial domain φ_j (x), (where x = x_1, x_2), of the basic Curvelet element is obtained from the Fourier transform of U_j. By rotation and translation of this basic Curvelet φ_j (x) at scale 2^{-j}, angle $\theta_{j,l}$ at position $x_k^{j,l}$, full Curvelet elements of different scales and orientations are derived (13).

$$\varphi_{j,l,k}(x) = \varphi_{j,0,0}\left(R_{\theta_{j,l}}\left(x - x_k^{j,l}\right)\right) \quad (13)$$

where j, l and k corresponds to scale, orientation and position, respectively. $R_\theta = \begin{pmatrix} \cos\theta & \sin\theta \\ -\sin\theta & \cos\theta \end{pmatrix}$ denotes the rotation matrix of angle θ.

The inner product of the Curvelet $\varphi_{j,l,k}$ and a function f provide continuous Curvelet coefficients (14).

$$C(j, l, k) := \langle f, \varphi_{j,l,k} \rangle \quad (14)$$

For discrete 2D digital images, a discrete transform called the FDCT was introduced [48]. It takes in a 2D image from a Cartesian array $I[m, n]$, where $0 \leq m < M, 0 \leq n < N$($M$ and N are dimensions of the array) and return a collection of digital Curvelet Coefficients $C^D(j, l, \text{k})$ indexed by scale j, orientation l and spatial location k = k_1, k_2 parameters (20). The approach is the application of a 2D forward Fourier transform at scale j and orientation l providing a wedge $U_{j,l}$.

The result is then wrapped around the origin and transformed with 2D inverse Fourier transform providing discrete Curvelet coefficients.

For the discrete Curvelet, band pass trapezoidal localized window $\left(U_j^D\right)$ is defined in the frequency domain using two windows equivalent to the continuous domain: the Cartesian $\left(W^D\right)$ and angular $\left(V^D\right)$ Windows. The W^D at scale j is derived from the difference of two low-pass windows in the frequency domain (ω)(15).

$$W_j^D(\omega) = \sqrt{\Phi_{j+1}^2(\omega) - \Phi_j^2(\omega)}, \quad j \geq j_0 \quad (15)$$

where Φ is the product of separable low-pass 1D window $\Phi_j(\omega_1, \omega_2) = \phi(2^{-j}\omega_1)\phi(2^{-j}\omega_2)$
The $V_j^D(\omega)$ is defined as:

$$V_j^D(\omega) = V_j^D\left(2^{\lfloor j/2 \rfloor}(\omega_2/\omega_1)\right) \quad (16)$$

From these two windows, the basic U_j^D with an equispaced slope $\tan\theta_l := l.2^{-\lfloor j/2 \rfloor}$ is defined as:

$$U_j^D(\omega) = 2^{-3j/4} W_j^D(\omega) V_j^D(\omega)$$
$$= 2^{-3j/4} W_j^D(\omega) V_j^D\left(S_{\theta_l}\omega\right) \quad (17)$$

where $S_\theta = \begin{bmatrix} 1 & 0 \\ -\tan\theta & 1 \end{bmatrix}$ is Cartesian shear matrix

Then, the scaled, sheared and translated trapezoidal wedges of corresponding cosine and sine Curvelet coefficients at each scale as reflection to each other and symmetry with respect to the origin are generated in the frequency domain (18). The Corresponding spatial domain is determined from (19).

$$U_{j,l,k}^D(\omega) = U_{j,0,0}^D\left(S_{\theta_l}\omega\right) * e^{-i\langle x_k^{j,l}, \omega\rangle} \quad (18)$$

$$\varphi_{j,l,k}^D(x) = \varphi_{j,0,0}^D\left(S_{\theta_l}^T\left(x - x_k^{j,l}\right)\right) \quad (19)$$

Consequently, a collection of the Curvelet coefficients, $C^D(j, l, \text{k})$ of an image $I[m, n]$ is obtained with the forward Curvelete transform (20).

$$C^D(j, l, \text{k}) = \sum_{\substack{0 \leq m < M \\ 0 \leq n < N}} I[m, n]\varphi_{(j,l,\text{k})}^D(m, n) \quad (20)$$

where superscript D stands for digital and $\varphi_{(j,l,\text{k})}^D$ is a digital Curvelet waveform
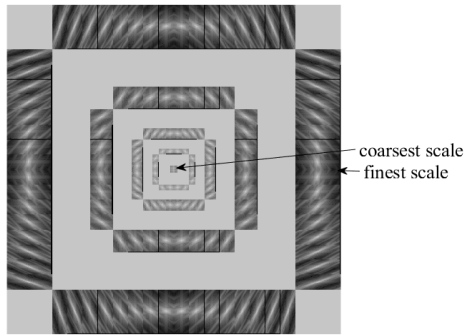
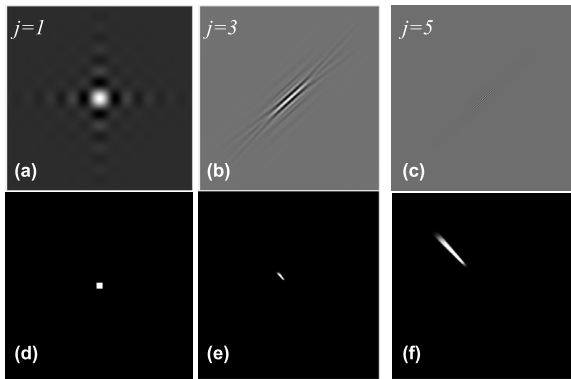**FIGURE 6.** Digital curvelet tiling of space and frequency.

FIGURE 7. Curvelets at scale *j*; (a)–(c) spatial, (d)–(f) the corresponding frequency domains.

The return $C^D(j, l, k)$ is a collection of frequency response coefficients arranged in to Cartesian coronae of four quadrants (North, East, South, West) each of which are arranged from coarse to fine outwards from center and separated in to rectangular tilings (Fig. 6).

At a given scale, the Curvelets are an oriented needle in space and a wedge in the frequency domain (Fig. 7) whose effective support is a rectangle obeying a parabolic relation of width $\approx$ length^2 [49]. At high frequency, they are fine and looks like needle shaped elements (Fig. 7(c)) and at low frequency they are none directional coarse elements (Fig. 7(a)).

The values of the Curvelet coefficient are determined by how the Curvelets are aligned in the image. Higher coefficients are expected when a Curvelet is accurately aligned to certain curve in an image. Fig. 8 shows an example of alignment of a Curvelet in relation to a curve in an image. In Fig. 8(a), the Curvelet is quite far from the curve alignment and therefore one can expect coefficient of zero value. In Fig. 8(b), the Curvelet intersected the curve and hence the coefficient would be a small none zero value. In Fig. 8(c), the Curvelet is almost perfectly aligned with the curved edge and therefore a high coefficient value is expected.

After selective manipulation of the Curvelets, the required output is recovered by employing inverse Curvelet transform (21).

$$I(m, n) = \sum_{j \geq j_0, l, k} C^D(j, l, k) \varphi^D_{j,l,k}(m, n) \qquad (21)$$
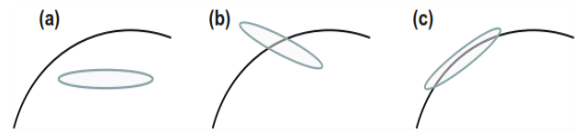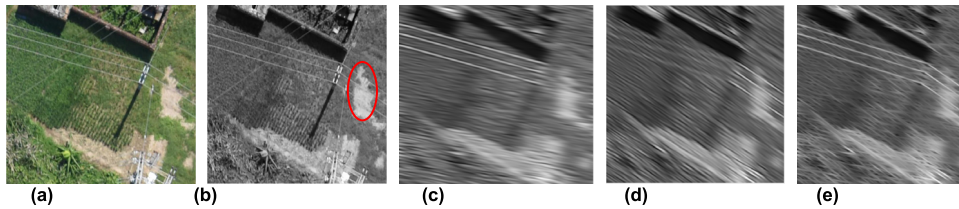

FIGURE 8. Alignment of curvelets in relation to curves.

Two implementations of FDCT were designed by [48]: the Unequally Spaced Fast Fourier Transform (USFFT) and wrapping methods. They differ mainly in the choice of spatial grid used to translate the Curvelets at each scale and orientation. The USFFT method is used to rotate the translation grid so as to align with the orientation of the Curvelet and the Curvelet coefficients at each scale and angle pair is then obtained by irregular sampling of the Fourier coefficients. The wrapping method involves periodizing the windowed frequency domain coefficients and re-indexing by wrapping it around a rectangle centered at the origin. It uses the same translation grid for every angle within each quadrant. Although, the output for both of the approaches is a table of digital Curvelet coefficients indexed by scale, orientation and spatial location parameters, the Wrapping method is easier. The details of these has been given in [47], [48], [50].

D. EXTRACTION AND REFINING

A well-established way to extract target features from images is thresholding. Depending on the pre-processing outputs and separablity of image features, different thresholding approaches were proposed. Image histogram properties (modality and evenness) were commonly used to determine single and multiple threshold values [51], [52]. Single thresholding may work for feature extraction from images of bi-modal histograms. However, due to gray level variation of an object across an image, it is unusual that single thresholding is successful always. The multi-thresholding methods were used for images of multi-modal histograms [53].

For images of unimodal histogram with no clear valley, dual thresholding is quite desirable. A faithful approach for dual thresholding, particularly, in the presence of noises or for images of filtering output is the hysteresis thresholding [54]. The hysteresis thresholding uses the spatial information of image features in addition to histogram information [55], [56]. It is a two-step approach: thresholding and connected component analysis and returns two threshold values, the high (T_H) and low (T_L) thresholds. The procedure is implemented in a way that a pixel P of an image $I_P(x, y)$ at location (x, y) is first classified as foreground (if strong), background or candidate (if weak) with reference to the threshold values and then will be checked for directional component connectivity. Any pixel or pixel difference below T_L is considered as background and discarded. Any pixel above T_H is considered as strong foreground and preserved. Intermediate pixels are then classified as candidates or weak foreground pixels based on connectedness. If a weak pixel is connected directly or through a path to a foreground, it is

M. E. Feyissa *et al.*: Integrated MGA Approach for Automatic Extraction of Power Lines From High Resolution Remote Sensing Images

IEEE *Access*

FIGURE 9. Gabor filter responses at $f = 0.088$; (a) original RGB image, (b) grayscale image, (c) filter response at $\theta = 56.25^0$, (d) filter response at $\theta = 78.75^0$ e) response of maximal combination.

TABLE 1. Basic information of the experimental images.

Image source	No. images	Pixel size
UAV	20	0.031m×0.031m
Onboard Helicopter	20	0.15m×0.15m
Google Earth	14	0.29m×0.29m

preserved by changing it in to foreground. Otherwise, it is made background and discarded [54].

$$I_p(x,y) = \begin{cases} foreground & if\ I_p\,(x,y) > T_H \\ background & if\ I_p\,(x,y) < T_L \\ candidate & otherwise \end{cases} \quad (22)$$

III. EXPERIMENTS

The experimental investigations were conducted on 48 high resolution real images with power lines. Due to the fineness of the power lines, the analysis was conducted on high resolution images: the UAV and the onboard helicopter captured images, and the streaming on demand Google Earth imagery [57]–[59] (Table 1). On the UAV images, power lines from both high tower and shorter electric poles were depicted. The rest possessed only high tower based power lines. Other six images (two from each of the above three sources) with no power lines were also used for the analysis.

The selection of the experimental images was made from the point of view of addressing the existing problems in extracting the power lines. The availability of the power lines associated with different noisy backgrounds and clutters, power lines crossing very high bright image regions and those represented with low contrast pixels were considered. Images with networked and multi-oriented power lines were also used to test the approach. The size of the experimental images varies based on the resolution and coverage.

In this section, the application of the experimental procedures on a sample image is presented. The experimental results conducted on the other test images are presented in section IV.

For the implementation of the experiment, first, a bank of 48 Gabor filters from 3 radial frequencies (f) corresponding to scale $\lambda = [2, 4, 8]$ and 16 orientations (θ) was used based on (5) and (6). These parameters were preferred based on the properties of the power lines. The λ values were

proposed from the fact that power lines are represented with few pixels. The number of θ was preferred to achieve optimum detection by reducing information loss. The generated Gabor filters were then applied over an UAV image of size 512×512 pixels following (5). The image depicts power lines oriented to different directions (Fig. 9(a)). It contains power lines that crossed very bright image regions and partly represented with low contrast pixels. Array of magnitude coefficients in which the image's pixels (x_i, y_i) represented by 48 dimensional feature vectors depicting the information of the subbands were obtained.

The Gabor response subbands were examined for their optimum information content (6) with respect to the parameters. The subbands with FBW=2.2 and AR=0.2 were found responding better at certain θ and f. More than one subbands were found containing optimum information. The output manifests that the better the filter's orientation matches the direction of the power lines, the better the power lines are discriminately enhanced. This implies that more than one Gabor filter is required to enhance multiorientation power lines. Although a single subband Gabor filter matching the direction of specific power lines improve the power lines globally, local structures are essentially better enhanced with multiple subband filters.

Fig. 9(a) depicts three power lines with directional change at the electric pole. The power lines are also crossing very bright and low contrast image regions. At these regions, the power lines were hardly identifiable. From filtering outputs presented in Fig. 9(c) – (d), for the same power line with changing direction, two filters with significant magnitudes in representing the power lines were found. One filter is derived from $f = 0.088$ oriented at $\theta = 56.25^0$. The output of the filter is presented in Fig. 9(c). It is clearly visible that parts of the power lines were enhanced well. However, the power lines over the very bright image region oriented to a different direction were not discriminated by this filter. The second filter with the same central frequency but oriented at $\theta = 78.75^0$ is found enhanced the other part of the power lines (Fig. 9(d)). Thus, it can be deduced that the maximal combination of two or more complementary subbands can provide an improved output. Fig. 9(e) shows the output of the maximal combination of the two filtering responses. It is clear now that the power line structures on both parts of the image were enhanced and the influence of the background objects were significantly reduced.
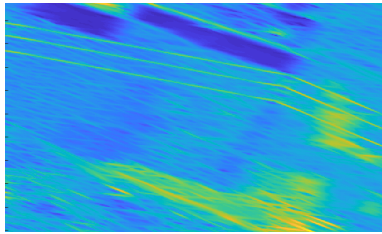
FIGURE 10. Maximally combined gabor response showing power lines represented by weak pixels and streaks introduced.
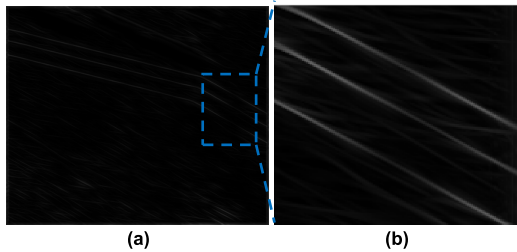
FIGURE 11. The matched filtering output; (a) the suppressed unnecessary background and noises by keeping the structures of the power lines (b) The zoomed in part of the brightness affected image region showing the discriminately filtered power lines.

However, the maximal combination of the different orientated filter response introduced some unnecessary short streaks (Fig. 10). Moreover, power lines crossing the very bright image regions and those represented with weak pixels were still not discriminated adequately. Therefore, we used the Gaussian template based MF (section *B*) to enhance discriminately.

The MF is adjustable based on the parameters used to estimate the dominant orientation, length and width of the power lines. In order to set the parameters, the properties of the power lines: the shape of the cross-section intensity profile, orientations, width and length were considered. They are thin (usually 1-5 pixels) and long, straight or very small curvature between two electric towers on the image. These properties are common for aerial and space born remote sensing images captured vertically. Based on these properties, the parameters and their respective values were determined. From series of experiments, the angular resolutions of 5^0, scale $\sigma = 0.5$ and $L = 15$ were found suitable. Thus, the MFs were generated and convolved with the output of the fused Gabor response according to (7-11). For each pixel only the maximum of the responses was retained. It can be seen from Fig. 11 that the effects of the background and the noises were significantly suppressed and the structures of the power lines were much better discriminated. The streak noises were also suppressed.

As Fig. 11shows, although most parts of the power lines can be discriminated from the background after applying complementary filters, resistant noises and weak pixels of the power lines still exist, which may still affect the eventual extraction. It has been defined in section *C* that the Curvelet transform is effective for selective modification of the image objects. Thus, the FDCT with the wrapping method was

preferred and employed over the Gabor-MF image using the Curvelab package (http://www.curvelet.org).

The Curvelet coefficients (20) were computed as $C \{j\} \{l\} (\mathbf{k})$. The total number of scales (J) was determined from the image's size (23).

$$J = \lceil log_2 (min (m \times n)) \rceil - 3 \qquad (23)$$
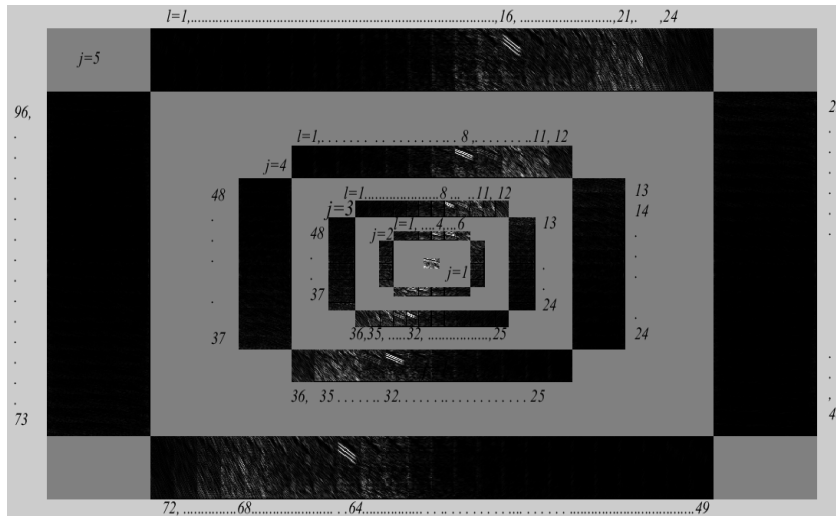
where $m \times n$ denotes the row by column sizes

Accordingly, the total number of scale for the experimental image was determined as $J = 6$. For angular decomposition, we have found in our experiment that 24 total number of orientations at $j = 2$ generated acceptable result. Thus, the angular decomposition of the wedges in each scale was computed by assigning $N_{l,j_2} = 24$, where N_{l,j_2} represent the number of orientation at the second scale. This is the first scale at which an angular decomposition begins. For $j \geq 2$, the angular decomposition is doubling in every second scale as $N = N_{l,j_2} \left(2^{\lceil j-2/2 \rceil}\right)$. Then the Curvelet transform was implemented over the image with real value coefficient option. The finest scale was preferred to be wavelet coefficient as a solution to issues related with under/over sampling as defined in [48] and [40].

The output Curvelet coefficients arranged as a digital Cartesian corona was obtained (Fig. 12). The inner most scale ($j = 1$) contains the smoothed version of the input formed by low frequency coefficients with no angular decomposition. From the second through the last scales, the Curvelets gets finer and finer. As the discrete forward Curvelet coefficients are represented at 4 quadrants, the N_l per quadrant became 6 at $j = 2$; both $j = 3$ and 4 have the same number of wedges $N_{l,j3,4} = 12$ per quadrant but differ with $\mathbf{k}$. At $j = 5$, $N_l = 24$ per quadrant. Scale $j = 6$ contains the finest wavelet derived high frequency coefficients with no angular decomposition. The wedges are arranged in a clockwise direction from northwest corner for each j.

The north-east quadrant wedges and the south-west were reflections of each other and symmetric around the center. For instance, in Fig. 12, the same power lines were represented at $j = 5, l = 16$ in the northern quadrant and at $j = 5, l = 64$ in the southern quadrant. It is also clearly visible that the Curvelet decomposition separately represented the power lines from other objects at specific j and l. They are well discriminated at j_4, l_8 and j_5, l_{16}.

Once the objects were represented separately, selective preserving and enhancement of the power lines and the suppression/removal of the unnecessary background and noises will be implemented. The scale $j = 1$ has low frequency and does not provide the geometric information of power lines (Fig. 13(a)). It includes the smooth background objects. Scale $j = 6$ contains isotropic and high frequency random noises (Fig. 13(b)).

The scale $j = 2$ was also found as less detailed providing less geometric information. Therefore, the scales $j = [1, 2, 6]$ were all shrunken to zero. The remaining coefficients at scales $j = [3, 4, 5]$ were found containing significant power line information (Fig. 12) and thus reserved.

M. E. Feyissa *et al.*: Integrated MGA Approach for Automatic Extraction of Power Lines From High Resolution Remote Sensing Images

IEEE *Access*

FIGURE 12. A set of curvelete coefficients with $J = 6$ and l trapezoidal wedges arranged in to four quadrants.
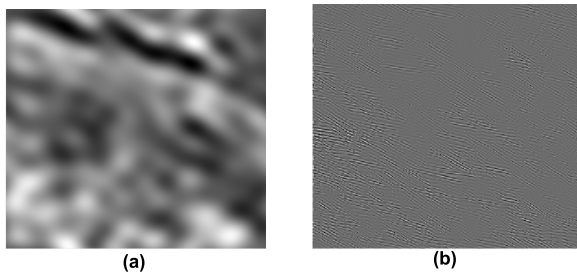
FIGURE 13. Reconstructed output; (a) $j = 1$ and (b) $j = 6$.

Now, the wedges of the reserved scales that contain optimum information needs to be identified and selected. Significant information for the image at hand was concentrated in the northern and the corresponding reflection in the southern quadrants. We preferred the northern quadrant and identified a set of wedges $\{j = 3, l \in [8, 11]\} \cup \{j = 4, l \in [8, 11]\} \cup \{j = 5, l \in [14, 22]\}$ containing optimum information. These trapezoidal wedges were reserved and all the rest were assigned with zero values. As shown in Fig. 14(a), in order to remove the remaining redundant objects, a threshold with a value of 0.6% was applied to the reserved coefficients. Finally, by implementing inverse FDCT, a much better improved power lines image with much better suppressed noises was reconstructed (Fig. 14(b)). It can be seen that almost all false lines were removed and the power lines even from the severely impaired part of the image were well recovered.

The multiscale and multiorientation methods implemented so far enabled the selective preservation and enhancement of the power lines effectively. The final operation is the segmentation and extraction of the power lines. The hysteresis thresholding (22) was used for the extraction. As two thresholding values (T_H and T_L) are required for the hysteresis thresholding, the histogram modality of the reconstructed image was examined to select the values. The histogram was unimodal and cannot be applied for threshold value determination. Therefore, the maximum value of the image was used as a starting value to determine T_H. T_H was derived by dividing the maximum value of the image to a constant and then T_L was obtained from dividing T_H to another constant. The constant value may vary from image to image.

For the experimental sample image, we used $T_H = \max(\text{real } (\text{IFCT}(x))/2$ and $T_L = T_H/2$. A binary image with zero values corresponding to the background and ones representing the power lines was obtained. Then, by refining some remaining small line segments using morphological functions, the power lines were extracted (Fig. 14(c)). The extracted lines were not uniform in thickness. However, lines representing same feature needs to be uniform. Using, morphological thinning operation [51], accurate power lines were generated. Fig. 14(d) presents the extraction output overlaying the original image. Based on the standard accuracy measures (described under section IV), the approach achieved 0.83, 0.85 and 0.99 completeness, correctness and quality measures, respectively.

IV. RESULT AND DISCUSSIONS

In this section the experimental application of the approach over the three image data sets (the UAV images, the onboard helicopter derived images and the Google maps) is demonstared to confirm the validity of the approach. For the sake of limiting space, sample experimental outputs from each of the three datasets were presented by zooming out their actual sizes. The presented images depicts power lines associated with different levels of background noises, clutters and brightness effects. The approach was also applied over images with no power lines to examine its contribution towards false positive values.

The output of each of the steps for each images is presented in Fig. 15. The first column is the grayscale original images. Fig. 15(a) is a UAV image of size 512×512 pixels possessing
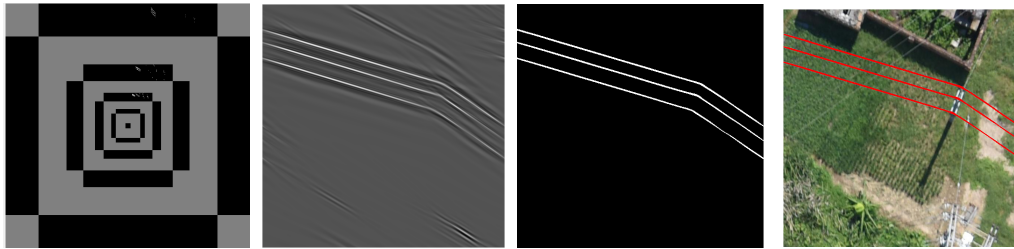
FIGURE 14. The digital curvelet transform and power lines extraction; (a) Digital cartesian representation of the reserved curvelet coefficients, (b) the reconstructed image, (c) the extracted power lines, (d) overlay the original image with the extraction output.

five horizontal oriented parallel power lines. It covers partly mixed vegetation with canopy shadows, randomly distributed noises and partly a bright contaminated low contrast region. Fig. 15(b) is a size of 512×512 pixels UAV image covering a very bright road, bright noises and mixed vegetation. The image depicts five parallel power lines with irregular distance from each other. The power lines were completely lost and look disconnected due to the brightness of the road. Moreover, the randomly distributed noises have intensity similar to the power lines posing discrimination challenges.

Fig. 15(c) shows an image with 700×700 pixels of onboard helicopter captured image. The image depicts power lines with mixed objects, bright tin roofs of buildings, bare land and low contrast pixels. Fig. 15(d) is a 1000×1000 pixels image of onboard helicopter. The image depicts power lines of low contrast pixels associated with mixed bright objects and varied land surface structures.

Fig. 15(e) shows Google Earth image of size 512×512 pixels illustrating 12 closer power lines. The power lines crossed low contrast image regions and associated mainly with bare land, sparse forest and brighter foot paths. Fig. 15(f) is also a Google Earth image of 900×900 pixels covering farmland associated with different surface structures. It depicts 12 power lines connected at the electric towers. The power lines coming from/radiating to different directions were connected at the towers. The high towers obstructed the connectivity of the power lines at the middle.

The second column shows the output of the maximal combination of the Gabor filtering response. It can be seen that the unnecessary backgrounds were suppressed and the power lines were improved to some extent. The level of enhancement of the power lines and suppression of the background varies based on the quality of the original images. For images with clear and distinctive power lines, pixels representing the power lines were discriminated better. For those image regions affected by brightness, associated with low contrasts and noises; the Gabor filtering was not enough. Some power lines pixels at low contrast and noisy regions were still weak. Some streak like structures were introduced and false lines parallel to the power lines were also enhanced. This is clearly visible on the second column of Fig. 15(a) and (e).

The third column shows the MF of the Gabor response images. At this step, pixels representing the power lines were

TABLE 2. Reserved scales *j* and orientations *l*.

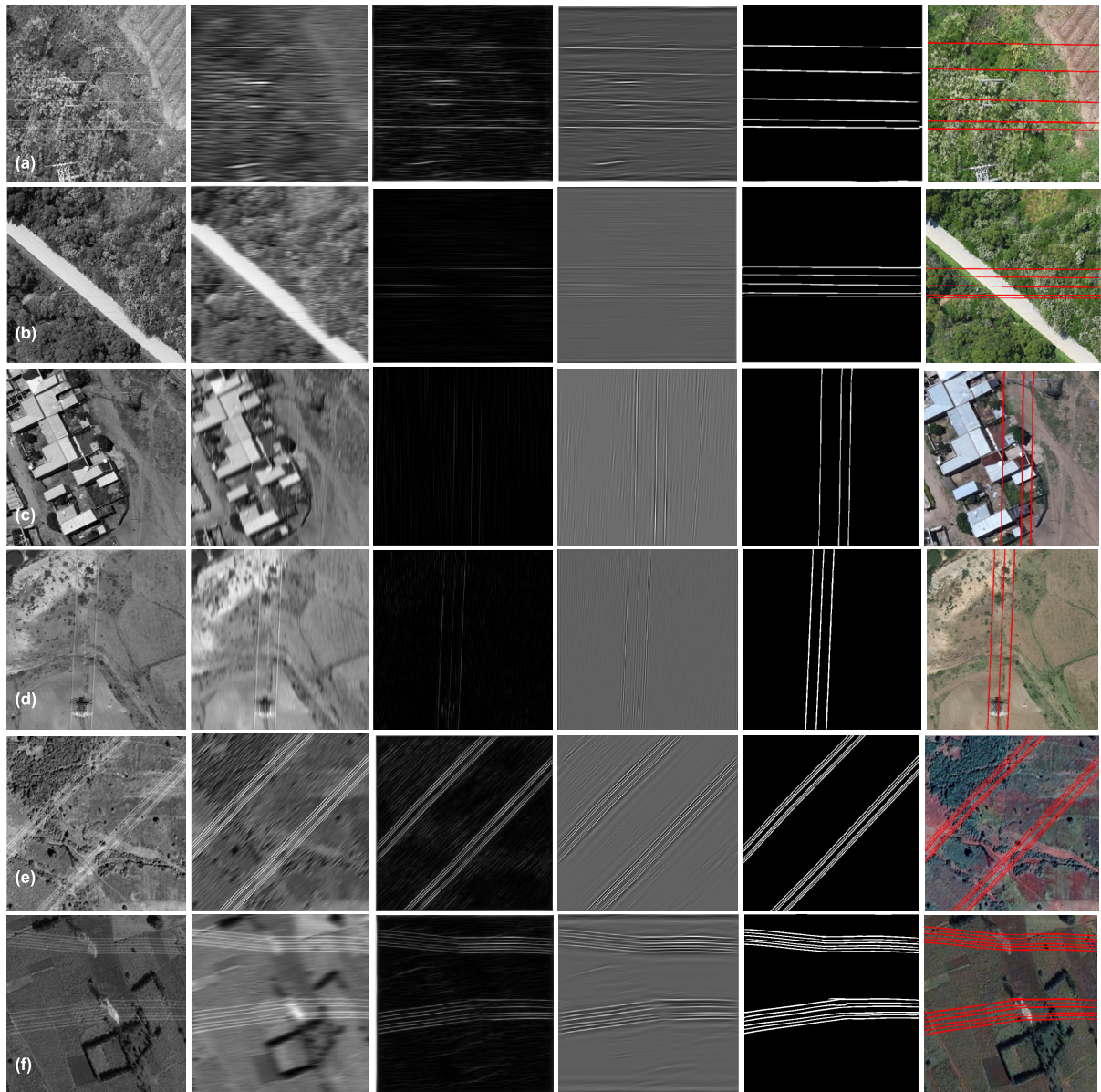| Image	Set of reserved j and l
a	$\{j=3, l \in [5,8]\} \cup \{j=4, l \in [5,8]\} \cup \{j=5, l \in [11,14]\}$
b	$\{j=3, l \in [5,7]\} \cup \{j=4, l \in [5,7]\} \cup \{j=5, l \in [10,13]\}$
c	$\{j=4, l \in [18,19]\} \cup \{j=5, l \in [36,37]\} \cup \{j=6, l \in [36,37]\}$
d	$\{j=4, l = 19\} \cup \{j=5, l = 37\} \cup \{j=6, l = 37\}$
e	$\{j=3, l \in [1,2]\} \cup \{j=4, l \in [1,2]\} \cup \{j=5, l \in [1,3]\}$
f	$\{j=4, l \in [5,7]\} \cup \{j=5, l \in [9,14]\} \cup \{j=6, l \in [9,14]\}$

discriminated well and the background noises and unnecessary objects were suppressed better. The connectivity of the power lines was also improved much better. This is particularly evident from the third column of Fig. 15(a), (b), (c) and (f) where the power lines were lost because of the brightness influences. But, still some resisting false lines were left.

The fourth column shows the outputs of the selective reconstruction of the reserved Curvelet transform coefficients derived from the MF outputs. Based on the respective size of the images different total numbers of scales (J) were obtained (23). The angular partitioning (number of angles) at the second coarsest scale was preferred as $j_2, l = 24$ for all the presented samples. The set of scales $\{j\}$ and wedges $\{l\}$ reserved corresponding to the sample images shown in Fig. 15 are given in Table 2.

Additional selective preservation was also implemented on the reserved coefficients for each image depending on the response. For all the presented sample images, 0.5% preservation was found working. Then the final enhancement outputs were recovered by applying the inverse FDCT. It can be seen that the unnecessary background and noises were suppressed and the required power lines were enhanced much better.

The fifth column shows the extracted and refined power lines by the hysteresis thresholding and morphological thinning operations. Finally, the extracted power lines were superimposed over the original RGB images and presented in the last column. One can realize visually that the extracted power lines are matching the power lines in the original images.

The automatically extracted power lines were evaluated quantitatively to determine how complete and correct the extracted power lines are with respect to the ground truth.

M. E. Feyissa *et al.*: Integrated MGA Approach for Automatic Extraction of Power Lines From High Resolution Remote Sensing Images

IEEE *Access*

FIGURE 15. The result of the experimental outputs. The first and the second row are the UAV images, the third and fourth are the onboard helicopter captured images and the fifth and sixth row are Google images. Column wise, from the first to the sixth column corresponds to the grayscale of the original image, the selectively maximally combined gabor filtering response, the output of the mf, the response of the curvelet transform, the final extraction result, and the overlaying of the extraction over the original RGB images; respectively.

We used the common standard discrepancy measures of completeness, correctness and quality used for line feature extraction [60], [61]. They are computed by generating the factors True Positive (TP), True Negative (TN), False Positive (FP) and False Negative (FN) numbers of pixels.

- $Completeness = \frac{TP}{TP+FP}$.
- $Correctness = \frac{TP}{TP+FN}$
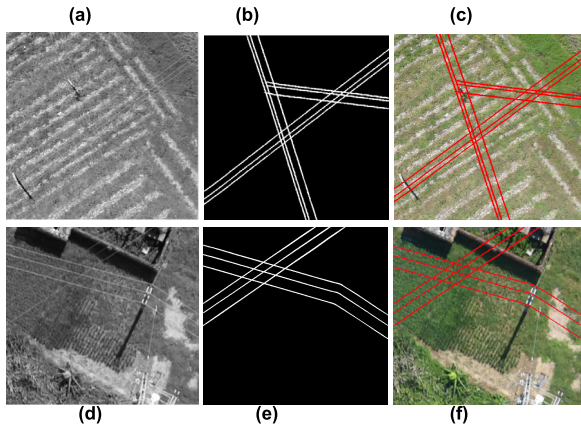- $Quality = \frac{TP+TN}{TP+FP+FN+TN}$

Accordingly, the accuracy of the approach over each of the experimental samples presented in Fig. 15 is evaluated by comparing the extraction output with the manually labeled ground truth data. The evaluation was carried out in two steps.

TABLE 3. Evaluation of the extraction outputs.

Measures	Images					
	a	b	c	d	e	f
Completeness	0.94	0.86	0.85	0.86	0.90	0.86
Correctness	0.80	0.81	0.88	0.89	0.83	0.87
Quality	0.99	0.99	0.99	0.99	0.98	0.98

First, matching factors were generated and then the accuracy measures were computed (Table 3).

For a good extraction, all the evaluation values are closer to 1. The completeness and correctness values are especially attractive measures of accuracy sensitive to over and

IEEE *Access*

M. E. Feyissa *et al.*: Integrated MGA Approach for Automatic Extraction of Power Lines From High Resolution Remote Sensing Images
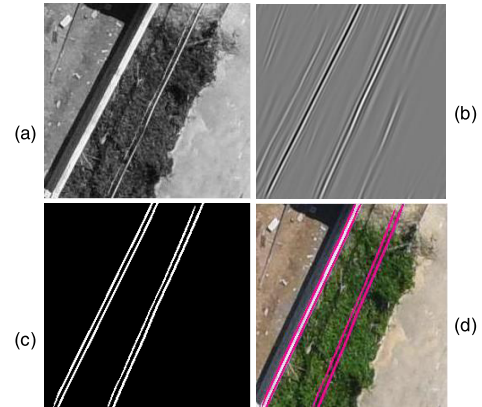

FIGURE 16. The networked and multi-oriented power lines. a) and d) Original images, b) and e) extraction output, c) and f) extracted power lines overlaying the original image.
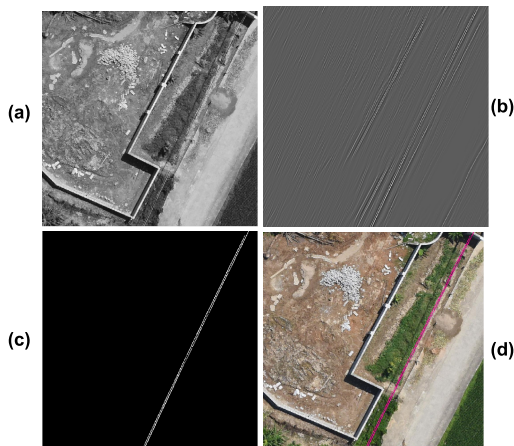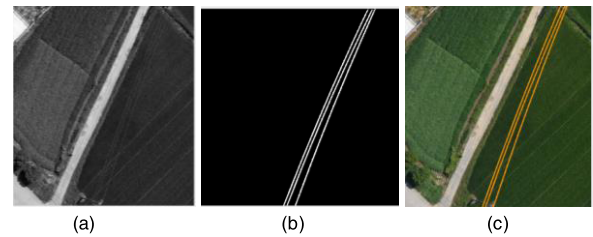

FIGURE 17. Power lines discrimination, a) original grayscale image, b) filtering and curvelet transform output, c) extraction output, d) Superimposing the original image.

FIGURE 18. Extraction of power lines from similar and equal image objects; (a) original grayscale image, (b) filtering and curvelet transform output, (c) extraction output, (d) superimposition.

FIGURE 19. Suppression of roads parallel to power lines, (a) grayscale image, (b) extracted power lines, (c) superimposition over the original RGB image.
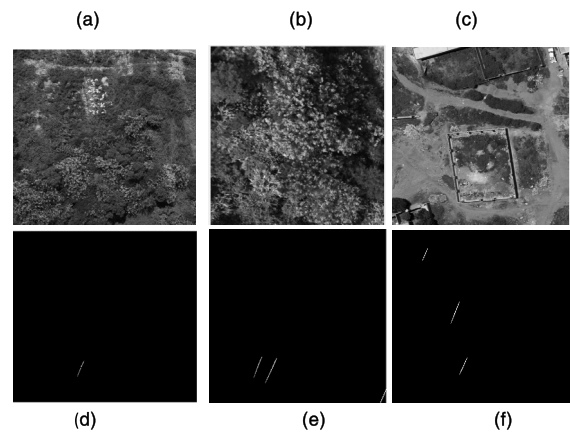
FIGURE 20. False positive outputs, (a)-(c) indicate original grayscale images, (d)-(f) shows the respective false positive pixels.

under-extraction. While over-extraction leads to low correctness scores, under-extraction leads to low completeness scores. Both yield high values if both the ground truth and the extracted output agree in location and level of detail. The quantitative results in table 3 corresponds to each of the images presented in Fig. 15. The completeness for all the images is over 0.86 which is quite good. The correctness ranges from 0.80-0.87 scores. The relatively lowest correctness score (0.80) is obtained from the image of Fig. 15(a). This is because of the fact that the original image was degraded and affected by the impacts of brightness, low contrast and noises. Thus, the power cables on the original image were poorly represented and hardly identified, especially on the affected part of the image. Concerning quality, the approach achieved over 0.98 scores which is quite good. Therefore, though there are differences based on the quality of the images, the approach provided satisfactory accuracy measures.
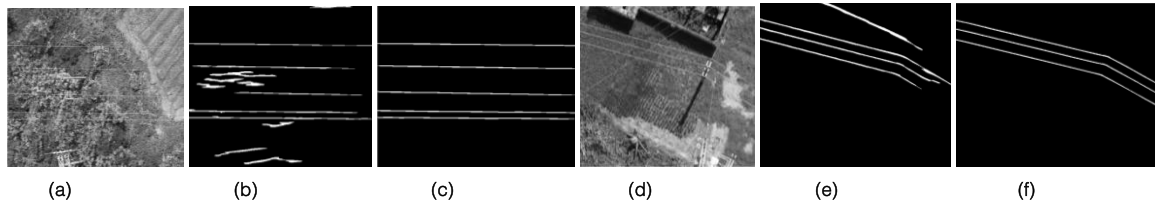
It has been presented in the first section that most of the existing approaches were orientation limited. Unlike those approaches, our approach achieved the detection and extraction of multi-oriented and network of power lines from a single image (Fig. 16). Fig. 16(a) presents an image depicting network of power lines oriented to different directions. The image shows power lines associated with background clutter and noise. Some parts of the power lines were seriously affected by high brightness. Some of them were represented by very weak intensity and cannot easily be discriminated. Fig. 16(d) shows the sample image presented earlier depicting multi-oriented power lines with changing direction. The effects of low contrast

M. E. Feyissa *et al.*: Integrated MGA Approach for Automatic Extraction of Power Lines From High Resolution Remote Sensing Images

IEEE *Access*

FIGURE 21. Comparison of outputs of direct FDCT and Gabor-MF-FDCT applications on two images; (a) and (d) are original grayscale images, (b) and (e) are extraction outputs from the direct application of FDCT, (c) and (f) The output of the Gabor-MF-FDCT approach.
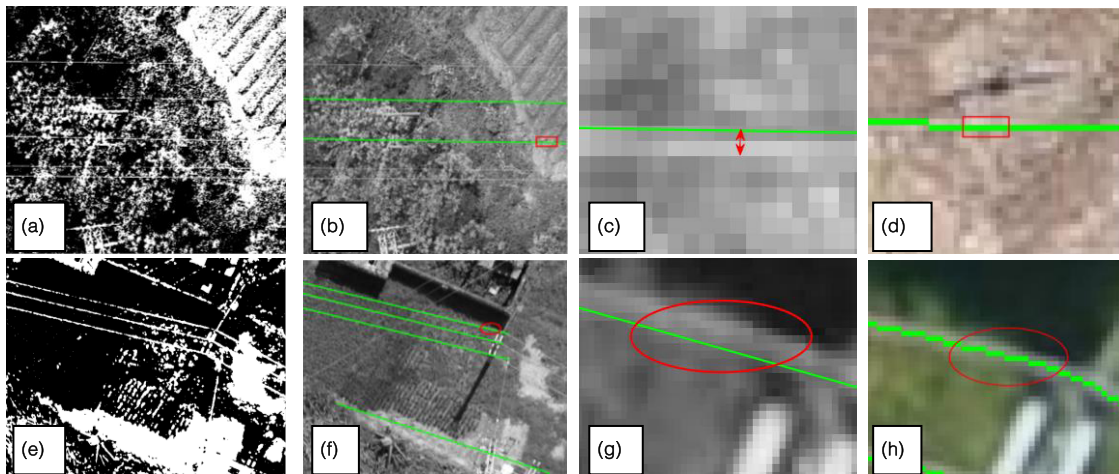
FIGURE 22. Output of the application of PCNN-Hough transform power line extraction, (a) and (e) the PCNN filter outputs, (b) and (f) the PCNN-Hough transform outputs superimposing the original gray-scale image, (c) and (g) shows comparative location of the power lines obtained with PCNN-Hough transform to the pixels representing power lines on the original images, (d) and (h) shows the comparative location of the power lines obtained with the Gabor-MF-FDCT approach to the orginal RGB image.

and brightness were also associated with this image. With the application of the approach, the multi-oriented power lines were effectively extracted from both of the images (Fig. 16(b)- (c) and (e) - (f).

The discrimination of power lines from objects similar and parallel to the power lines was also mentioned as one of the challenges to extract them. Power lines are thin, usually stretched over longer distance and they are little curve to straight between two poles. Our approach exploited these properties to selectively enhance and preserve the power lines and to remove the other similar unnecessary parallel objects.

Fig. 17(b) shows that both power lines and parallel fences are detected at the first place. With step by step filtering and Curvelet transform, the fence was subdivided in to smaller pieces and finally removed.

However, for shorter and straight power lines associated with similar and parallel linear objects exactly equal in length, the separate discrimination and extraction still remains challenging. Fig. 18 presents part of the image in Fig. 17 showing a fence with two parallel edges located parallel to the power lines. The edges of the fence have equal length and look similar with the power lines. Using our approach with the same parameters used above, the outputs of filtering and Curvelet transform (Fig. 18(b)), and the extraction output (Fig. 18(c)) could not separate them.

Therefore, for images with shorter and straight power lines associated with exactly equal, similar and parallel objects, the approach can respond higher false positive value and thus not adequate to separately extract the power lines. This problem will be investigated in our future study.

Objects equal in length with the power lines but differ in width can be suppressed using the complementary qualities of the Gabor filter with the FBW and AR parameters, and the scale based MF. Fig. 19 shows a road depicted parallel to the power lines. It can be seen that (Fig. 19(b) the road is removed leaving the power lines.

The proposed approach is effective for orientation based reduction of false positive pixels. Fig. 20 shows the response of our approach over three sample images (from the three sources) with no power lines. As the images do not depict any power lines to determine the parameters, the same filtering, Curvelet transform and hysteresis thresholding parameters used for the image with power lines presented above (Fig. 19) were used as a benchmark for this demonstration. However, the refinement operations were not employed here.

Obviously, false positive pixels were produced. However, the numbers of the false positive pixels are quite low. For the three sample images, the number of false positive pixels produced were 219 (0.022%), 516 (0.11%), and 356 (0.09%) respectively. As power lines have some particular properties,

IEEE Access

M. E. Feyissa *et al.*: Integrated MGA Approach for Automatic Extraction of Power Lines From High Resolution Remote Sensing Images

most of the false alarms can easily be identified and managed using the proposed refinement operations.

Though, the data available in literatures do not permit sufficient comparison of our approach with other approaches, an attempt was made to compare with some two other approaches: the extraction output from the direct application of FDCT and the PCNN-Hough transform approaches. Fig. 21 shows the comparative outputs of the direct application of FDCT to the Gabor filtered-MF- FDCT based power line extraction. It can be seen that in both Fig. 21(b) and (e), the structures of the power lines were broken and incomplete. Moreover, the false alarms (unwanted noises) were hardly removed. These problems are well addressed by the Gabor-MF- FDCT approach in that the structures of the power lines were extracted very well Fig. 21(c) and (f)).

Also, the output of the application of the PCNN-Hough transform based power lines enhancement and extraction is shown in Fig. 22. For these experimental images, the application of the PCNN-Hough transform in extracting the power lines looks unsatisfactory. Although some pixels corresponding to the power lines right orientated diagonal were pulsed well over most of the background pixels (Fig. 22(a) and (e)), background pixels over bright regions crossed by the power lines and some other regions were also pulsed in the same way. On the other hand, power line pixels with low intensity oriented up-right diagonal were all removed. It can be seen that the power line structures are only partially recovered (Fig. 22(b) and (f)) and the positions of those extracted power lines by the PCNN-Hough transform are also inaccurate (Fig. 22(c) and (g)). In comparison, the Gabor-MF-FDCT approach (Fig. 22(d) and (h)) showed complete and accurate extraction output and thus showed quite superior performance.

V. CONCLUSION

The development of high resolution remote sensing systems enabled the acquisition of finer resolution images. These images provide potentials for extracting finer spatial features. This paper presented a novel approach for automatic extraction of power lines from high resolution remote sensing images. The proposed approach involves complementary MGA tools and extraction methods. The experimental result revealed that the approach is capable of extracting power lines from high resolution images of different sources and captured from different orientations. It is robust in extracting power lines represented with weak pixels, power lines crossing bright regions, and those networked and curved power lines with changing orientation. It derived power line structures from disconnected/broken image regions caused by noise effectively. Further researches are needed to improve the performance.

ACKNOWLEDGMENT

REFERENCES

[1] H. Guan, Y. Yu, J. Li, Z. Ji, and Q. Zhang, "Extraction of power-transmission lines from vehicle-borne lidar data," *Int. J. Remote Sens.*, vol. 37, no. 1, pp. 229–247, Jan. 2016.

[2] J. Oh and C. Lee, "3D power line extraction from multiple aerial images," *Sensors*, vol. 17, no. 10, p. 2244, 2017.

[3] Y. Chen, Y. Li, H. Zhang, L. Tong, Y. Cao, and Z. Xue, "Automatic power line extraction from high resolution remote sensing imagery based on an improved radon transform," *Pattern Recognit.*, vol. 49, pp. 174–186, Jan. 2016.

[4] R. Bhola, N. H. Krishna, K. N. Ramesh, J. Senthilnath, and G. Anand, "Detection of the power lines in UAV remote sensed images using spectral-spatial methods," *J. Environ. Manage.*, vol. 206, pp. 1233–1242, Jan. 2018.

[5] G. Yan, C. Li, G. Zhou, W. Zhang, and X. Li, "Automatic extraction of power lines from aerial images," *IEEE Geosci. Remote Sens. Lett.*, vol. 4, no. 3, pp. 387–391, Jul. 2007.

[6] Z. Li, Y. Liu, R. Walker, R. Hayward, and J. Zhang, "Towards automatic power line detection for a UAV surveillance system using pulse coupled neural filter and an improved Hough transform," *Mach. Vis. Appl.*, vol. 21, no. 5, pp. 677–686, Aug. 2010.

[7] T. Santos, M. Moreira, J. Almeida, A. Dias, A. Martins, J. Dinis, J. Formiga, and E. Silva, "PLineD: Vision-based power lines detection for unmanned aerial vehicles," in *Proc. IEEE Int. Conf. Auto. Robot Syst. Competitions (ICARSC)*, Apr. 2017, pp. 253–259.

[8] J. Zhang, L. Liu, B. Wang, X. Chen, Q. Wang, and T. Zheng, "High speed automatic power line detection and tracking for a UAV-based inspection," in *Proc. Int. Conf. Ind. Control Electron. Eng. (ICICEE)*, Aug. 2012, pp. 266–269.

[9] C. Mu, J. Yu, Y. Feng, and J. Cai, "Power lines extraction from aerial images based on Gabor filter," in *Proc. SPIE*, vol. 7492, pp. 1–8, Oct. 2009.

[10] B. Song and X. Li, "Power line detection from optical images," *Neuro-computing*, vol. 129, pp. 350–361, Apr. 2014.

[11] K. N. Ramesh, A. S. Murthy, J. Senthilnath, and S. N. Omkar, "Automatic detection of powerlines in UAV remote sensed images," in *Proc. IEEE CATCON*, Dec. 2015, pp. 17–21.

[12] A. Ceron, I. F. Mondragon B., and F. Prieto, "Power line detection using a circle based search with UAV images," in *Proc. Int. Conf. Unmanned Aircr. Syst. (ICUAS)*, May 2014, pp. 632–639.

[13] Y. Zhang, X. Yuan, W. Li, and S. Chen, "Automatic power line inspection using UAV images," *Remote Sens.*, vol. 9, no. 8, p. 824, 2017.

[14] A. K. Jain and F. Farrokhnia, "Unsupervised texture segmentation using Gabor filters," *Pattern Recognit.*, vol. 24, no. 12, pp. 1167–1186, Jan. 1991.

[15] T. Andrysiak and M. Choras, "Image retrieval based on hierarchical Gabor filters," *Int. J. Appl. Math. Comput. Sci.*, vol. 15, no. 4, pp. 471–480, 2005.

[16] S. Bera, M. Sharma, and B. Singh, "Feature extraction and analysis using Gabor filter and higher order statistics for the JPEG steganography," *Int. J. Appl. Eng. Res.*, vol. 13, no. 5, pp. 2945–2954, 2018.

[17] Z. Ibtissam, C. Brahim, and M. Lhoussaine, "Building detection using local Gabor feature," *Int. J. Comput. Appl.*, vol. 181, no. 33, pp. 17–20, 2018.

[18] F. Yang and R. Lishman, "Land cover change detection using Gabor filter texture," in *Proc. 3rd Int. Workshop Texture Anal. Synth.*, 2003, vol. 2, no. 3, pp. 1–5.

[19] L. Chen, Q. Zhu, X. Xie, H. Hu, and H. Zeng, "Road extraction from VHR remote-sensing imagery via object segmentation constrained by Gabor features," *ISPRS Int. J. Geo-Inf.*, vol. 7, no. 9, p. 362, 2018.

[20] X. Chen and W. Huang, "Identification of rain and low-backscatter regions in X-band marine radar images: An unsupervised approach," *IEEE Trans. Geosci. Remote Sens.*, to be published.

[21] A. C. Bovik, M. Clark, and W. S. Geisler, "Multichannel texture analysis using localized spatial filters," *IEEE Trans. Pattern Anal. Mach. Intell.*, vol. 12, no. 1, pp. 55–73, Jan. 1990.

[22] V. Kyrki, J.-K. Kämäräinen, and H. Kälviäinen, "Simple Gabor feature space for invariant object recognition," *Pattern Recognit. Lett.*, vol. 25, no. 3, pp. 311–318, Feb. 2004.

[23] J.-K. Kämäräinen, V. Kyrki, and H. Kälviäinen, "Invariance properties of Gabor filter-based features-overview and applications," *IEEE Trans. Image Process.*, vol. 15, no. 5, pp. 1088–1099, May 2006.

[24] F. Bianconi and A. Fernández, "Evaluation of the effects of Gabor filter parameters on texture classification," *Pattern Recognit.*, vol. 40, no. 12, pp. 3325–3335, Dec. 2007.

[25] Y. Rubner and C. Tomasi, *Perceptual Metrics for Image Database Navigation*. Norwell, MA, USA: Kluwer, 2001.

M. E. Feyissa *et al.*: Integrated MGA Approach for Automatic Extraction of Power Lines From High Resolution Remote Sensing Images

IEEE *Access*

[26] L. Chen, G. Lu, and D. Zhang, "Effects of different Gabor filter parameters on image retrieval by texture," in *Proc. 10th Int. Multimedia Modeling Conf. (MMM)*, 2004, pp. 273–278.

[27] J. Ilonen, J.-K. Kämäräinen, and H. Kälviäinen, "Efficient computation of Gabor features," Dept. Inf. Technol., Lappeenranta Univ. Technol., Lappeenranta, Finland, Res. Rep. 100, 2005.

[28] J. Kämäräinen, V. Kyrki, and H. Kälviäinen, "Fundamental frequency Gabor filters for object recognition," in *Proc. 16th Int. Conf. Pattern Recognit.*, 2002, pp. 628–631.

[29] S. E. Grigorescu, N. Petkov, and P. Kruizinga, "Comparison of texture features based on Gabor filters," *IEEE Trans. Image Process.*, vol. 11, no. 10, pp. 1160–1167, Oct. 2002.

[30] S. V. Vaseghi, *Advanced Digital Signal Processing and Noise Reduction*, 3rd ed. West Sussex, Shire: Wiley, 2006.

[31] G. B. Giannakis and M. K. Tsatsanis, "Signal detection and classification using matched filtering and higher order statistics," *IEEE Trans. Acoust., Speech, Signal Process.*, vol. 38, no. 7, pp. 1284–1296, Jul. 1990.

[32] T. S. Murphy, M. J. Holzinger, and B. Flewelling, "Space object detection in images using matched filter bank and Bayesian update," *J. Guid., Control, Dyn.*, vol. 40, no. 3, pp. 497–509, Mar. 2017.

[33] M. Zhang and L. Wen, "An effective method for small event detection: Match and locate (M&L)," *Geophys. J. Int.*, vol. 200, no. 3, pp. 1523–1537, 2015.

[34] Y. Shi, Z. Nenadic, and X. Xu, "Novel use of matched filtering for synaptic event detection and extraction," *PLoS ONE*, vol. 5, no. 11, 2010, Art. no. e15517.

[35] B. Zhang, L. Zhang, L. Zhang, and F. Karray, "Retinal vessel extraction by matched filter with first-order derivative of Gaussian," in *Proc. Int. Symp. Vis. Comput., Adv. Vis. Comput. (ISVC)*, in Lecture Notes in Computer Science, 2011, pp. 410–420.

[36] M. Al-Rawi, M. Qutaishat, and M. Arrar, "An improved matched filter for blood vessel detection of digital retinal images," *Comput. Biol. Med.*, vol. 37, no. 2, pp. 262–267, Feb. 2007.

[37] S. Chaudhuri, S. Chatterjee, N. Katz, M. Nelson, and M. Goldbaum, "Detection of blood vessels in retinal images using two-dimensional matched filters," *IEEE Trans. Med. Imag.*, vol. 8, no. 3, pp. 263–269, Sep. 1989.

[38] M. Greitans, M. Pudzs, and R. Fuksis, "Object analysis in images using complex 2D matched filters," in *Proc. IEEE EUROCON*, May 2009, pp. 1392–1397.

[39] M. S. Nixon and A. S. Aguado, *Feature Extraction and Image Processing*, 2nd ed. London, U.K.: Elsevier, 2008.

[40] A. Tzanis, "The curvelet transform in the analysis of 2-D GPR data: Signal enhancement and extraction of orientation-and-scale-dependent information," *J. Appl. Geophys.*, vol. 115, pp. 145–170, Apr. 2015.

[41] P. T. Gallagher, C. A. Young, J. P. Byrne, and R. T. J. McAteer, "Coronal mass ejection detection using wavelets, curvelets and ridgelets: Applications for space weather monitoring," *Adv. Space Res.*, vol. 47, no. 12, pp. 2118–2126, Jun. 2011.

[42] W.-C. Lin, C.-C. Li, J. I. Epstein, and R. W. Veltri, "Curvelet-based texture classification of critical gleason patterns of prostate histological images," in *Proc. IEEE 6th Int. Conf. Comput. Adv. Bio Med. Sci. (ICCABS)*, Pittsburgh, PA, USA, Oct. 2016, pp. 1–6.

[43] A. A. Patil and J. Singhai, "Image denoising using curvelet transform: An approach for edge preservation," *Sci. Ind. Res.*, vol. 69, no. 1, pp. 34–38, 2010.

[44] S. Farzam and M. Rastgarpour, "An image enhancement method based on curvelet transform for CBCT-images," *Int. J. Comput. Inf. Eng.*, vol. 11, no. 6, pp. 215–221, 2017.

[45] A. Schmitt, B. Wessel, and A. Roth, "An innovative curvelet-only-based approach for automated change detection in multi-temporal SAR imagery," *Remote Sens.*, vol. 6, no. 3, pp. 2435–2462, 2014.

[46] D. Devapal, N. Hashna, V. P. Aparna, C. Bhavyasree, J. Mathai, and K. S. Soman, "Object detection from SAR images based on curvelet despeckling," *Mater. Today, Proc.*, vol. 11, pp. 1102–1116, Jan. 2019.

[47] J. Ma and G. Plonka, "The curvelet transform: A review of recent applications," *IEEE Signal Process. Mag.*, vol. 27, no. 2, pp. 118–133, Mar-2010.

[48] E. Candés, L. Demanet, D. Donoho, and L. Ying, "Fast discrete curvelet transforms," *Multiscale Model. Simul.*, vol. 5, no. 3, pp. 861–899, Jan. 2006.

[49] L. Ying, L. Demanet, and E. Candes, "3D discrete curvelet transform," in *Proc. SPIE*, vol. 5914, pp. 1–11, Sep. 2005.

[50] J.-L. Starck, F. Murtagh, and J. M. Fadili, *Sparse Image and Signal Processing: Wavelets and related Geometric Multiscale Analysis*, 2nd ed. New York, NY, USA: Cambridge Univ. Press, 2015.

[51] R. C. Gonzalez and R. E. Woods, *Digital Image Processing*, 3rd ed. Upper Saddle River, NJ, USA: Prentice-Hall, 2008.

[52] T. Acharya and A. K. Ray, *Image Processing: Principles and Applications*. Hoboken, NJ, USA: Wiley, 2005.

[53] M. Sonka, V. Hlavac, and R. Boyle, *Image Processing, Analysis and Machine Vision*, 1st ed. London, U.K.: Chapman & Hall, 1993.

[54] M. Al Najjar, M. Ghantous, and M. Bayoumi, "Hysteresis Thresholding," in *Video Surveillance for Sensor Platforms: Algorithms and Architectures* (Lecture Notes in Electrical Engineering), vol. 114, M. Al Najjar, M. Ghantous, and M. Bayoumi, Eds. New York, NY, USA: Springer, 2014, pp. 147–151.

[55] R. Medina-Carnicer, F. J. Madrid-Cuevas, A. Carmona-Poyato, and R. Muñoz-Salinas, "On candidates selection for hysteresis thresholds in edge detection," *Pattern Recognit.*, vol. 42, no. 7, pp. 1284–1296, Jul. 2009.

[56] N. Coudray, J.-L. Buessler, and J.-P. Urban, "Robust threshold estimation for images with unimodal histograms," *Pattern Recognit. Lett.*, vol. 31, no. 9, pp. 1010–1019, Jul. 2010.

[57] Q. Hu, W. Wu, T. Xia, Q. Yu, P. Yang, Z. Li, and Q. Song, "Exploring the use of Google earth imagery and object-based methods in land use/cover mapping," *Remote Sens.*, vol. 5, no. 11, pp. 6026–6042, 2013.

[58] K. Malarvizhi, S. V. Kumar, and P. Porchelvan, "Use of high resolution Google Earth satellite imagery in landuse map preparation for urban related applications," *Procedia Technol.*, vol. 24, pp. 1835–1842, Jan. 2016.

[59] A. Farah, "GoogleEarth for precision agriculture (Aswan, Egypt)," *Agricult. Eng. Int., CIGR J.*, vol. 19, no. 5, pp. 1–5, 2017.

[60] H. M. Christian Wiedemann and C. Heipke, "Emperical evaluation of automatically extracted road axes," in *Proc. CVPR Workshop Empirical Eval. Methods Comput. Vis.*, 1998, pp. 172–187.

[61] C. Poullis and S. You, "Delineation and geometric modeling of road networks," *ISPRS J. Photogram. Remote Sens.*, vol. 65, no. 2, pp. 165–181, Mar. 2010.

MULETA EBISSA FEYISSA received the M.Sc. degree in remote sensing and geo-information science from Addis Ababa University, Ethiopia, in 2009. Since 2009, he has been a Lecturer and a Researcher with the Department of Earth Sciences, Wollega University, Ethiopia. He is currently pursuing the Ph.D. degree in geographic information engineering with the Collage of Geological Engineering and Surveying, Chang'an University, Xi'an China. His research interests include geographic information analysis and mapping, geospatial data derivation, remote sensing image analysis, and segmentation and feature extraction.

JIANNONG CAO received the Ph.D. degree from Wuhan University, Wuhan, China, in 2005. He is currently a Professor and a Doctoral Tutor with the School of Earth Science and Resources, Chang'an University, Xi'an, China. His research interests include image understanding and image pattern recognition, high resolution remote sensing information extraction technology, remote sensing technology and application, geographic information system and application, Lidar point cloud information extraction, and 3S basic theory and technology application.
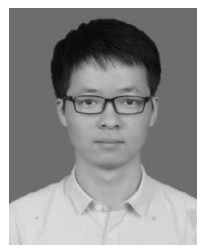
JUNJUN LI is currently a Doctoral Student with the School of Earth Science and Resources, Chang'an University, Xi'an, China. His research interests include high resolution remotely sensed image processing, spatial feature extraction, image segmentation, pattern recognition, deep learning, and remote sensing applications.

• • •